

Deterministic Scheme for Type-II Dirac Points and Experimental Realization in Acoustics

Xiaoxiao Wu¹, Xin Li², Ruo-Yang Zhang¹, Xiao Xiang², Jingxuan Tian³, Yingzhou
Huang², Shuxia Wang², Bo Hou^{4,5}, C. T. Chan¹, Weijia Wen^{1,6,a)}

¹*Department of Physics, The Hong Kong University of Science and Technology, Clear
Water Bay, Kowloon, Hong Kong, China*

²*Chongqing Key Laboratory of Soft Condensed Matter Physics and Smart Materials,
College of Physics, Chongqing University, Chongqing 400044, China*

³*Department of Mechanical Engineering, Faculty of Engineering, The University of
Hong Kong, Hong Kong, China*

⁴*School of Physical Science and Technology & Collaborative Innovation Center of
Suzhou Nano Science and Technology, Soochow University, Suzhou 215006, China*

⁵*Key Laboratory of Modern Optical Technologies of Ministry of Education & Key Lab
of Advanced Optical Manufacturing Technologies of Jiangsu Province, Suzhou
215006, China*

⁶*Materials Genome Institute, Shanghai University, Shanghai 200444, China*

^{a)}Correspondence and requests for materials should be addressed to Weijia Wen (email:
phwen@ust.hk).

Abstract

Low-energy electrons near Dirac/Weyl nodal points mimic massless relativistic fermions. However, as they are not constrained by Lorentz invariance, they can exhibit tipped-over type-II Dirac/Weyl cones which provide highly anisotropic physical properties and responses, creating unique possibilities. Recently, they have been observed in several quantum and classical systems. Yet, there is still no simple and deterministic strategy to realize them since their nodal points are accidental degeneracies, unlike symmetry-guaranteed type-I counterparts. Here, we propose a band-folding scheme for constructing type-II Dirac points, and we use a tight-binding analysis to unveil its generality and deterministic nature. Through a realization in acoustics, type-II Dirac points are experimentally visualized and investigated using near-field mappings. As a direct effect of tipped-over Dirac cones, strongly tilted kink states originating from their valley-Hall properties are also observed. This deterministic scheme may serve as a basis for further investigations of intriguing physics associated with type-II Dirac/Weyl points.

Introduction

In condensed matters, low-energy electrons around two/three-dimensional (2D/3D) Dirac/Weyl points mimic massless fermions in high-energy physics. However, since the stringent Lorentz invariance is absent in a lattice due to the breaking of continuous rotational symmetry [1], their two/three-dimensional (2D/3D) Dirac/Weyl cones can be tilted, which is first noted in various Dirac materials such as

strained graphene[2,3]. If the tilt becomes strong enough to tip over the cones in a specific direction, type-II Dirac/Weyl points (DPs/WPs) arise, with the nodal points, originally isolated (Fermi surface of type-I DPs/WPs), becoming contacts of electron-like and hole-like Fermi pockets [4-11]. Such topological transitions of the Fermi surfaces lead to highly anisotropic optical [6,10], magnetic [5,11], and electrical [7,8] properties. In fact, this topological transition are not unique to band structures of electronic materials, and should be realizable for any type of Bloch modes. Very recently, they have been proposed in classical systems [12-21], and experimentally demonstrated [16,17,20]. However, as accidental degeneracies, 2D type-II DPs, if exist, will only emerge at hardly predictable low-symmetry points in the reciprocal space, and they still lacks generally applicable design strategies, not to mention the more complicated 3D type-II WPs. In contrast, type-I DPs are guaranteed to exist at corners of the first Brillouin zone (FBZ) using triangular, honeycomb, or kagome lattices [22]. This property serves as a basis for further researches of many (pseudo)relativistic and topological phenomena associated with type-I DPs, such as the Klein tunneling [23,24], the *Zitterbewegung* effect [25-27], and various topological insulators [28-34].

In this work, to provide type-II DPs such a simple and robust platform for further researches, we introduce a deterministic construction scheme based on the band-folding mechanism [28], with its physics illustrated using a general tight-binding model. A direct experimental realization in acoustics are demonstrated, in which sonic crystals comprising bow-tie shaped holes are investigated using

near-field mappings. The dispersions of the type-II DPs are clearly resolved, featuring the deterministic contacts between electron-like and hole-like Fermi pockets. Strongly tilted valley-Hall kink modes, a direct manifestation of tipped-over Dirac cones, are also directly observed. The experimental results achieve quantitative agreement with theoretical and numerical predictions. The deterministic scheme could serve as a basis for investigating (pseudo)relativistic and topological phenomena of type-II DPs, and may boost more systematic designs of (synthetic) type-II WPs.

Results

We begin explaining our scheme from a sonic crystal as shown in Fig. 1(a). It comprises bow-tie shaped holes (details in the inset), arranged in a rectangular lattice, drilled on an acoustic-hard plate immersed in air. A primitive cell of the sonic crystal is denoted by the shaded green region. The first resonant mode of each single hole is an s -orbital cavity mode, anisotropic because of the bow-tie shape [18]. Polaritonic couplings [35,36] between plane waves and these s -orbital cavity modes give rise to spoof surface acoustic wave (SSAW) modes, forming the 1st band of the sonic crystal (see Fig. S1 in Supplementary Material [37]). Conveniently, we choose following geometric parameters, lattice constants $a_x/2 = 12.5$ mm and $a_y = 16$ mm, depth of holes $h = 10$ mm, and bow-tie shape $l_x = 7$ mm, $l_y = 14$ mm, $w = 3$ mm.

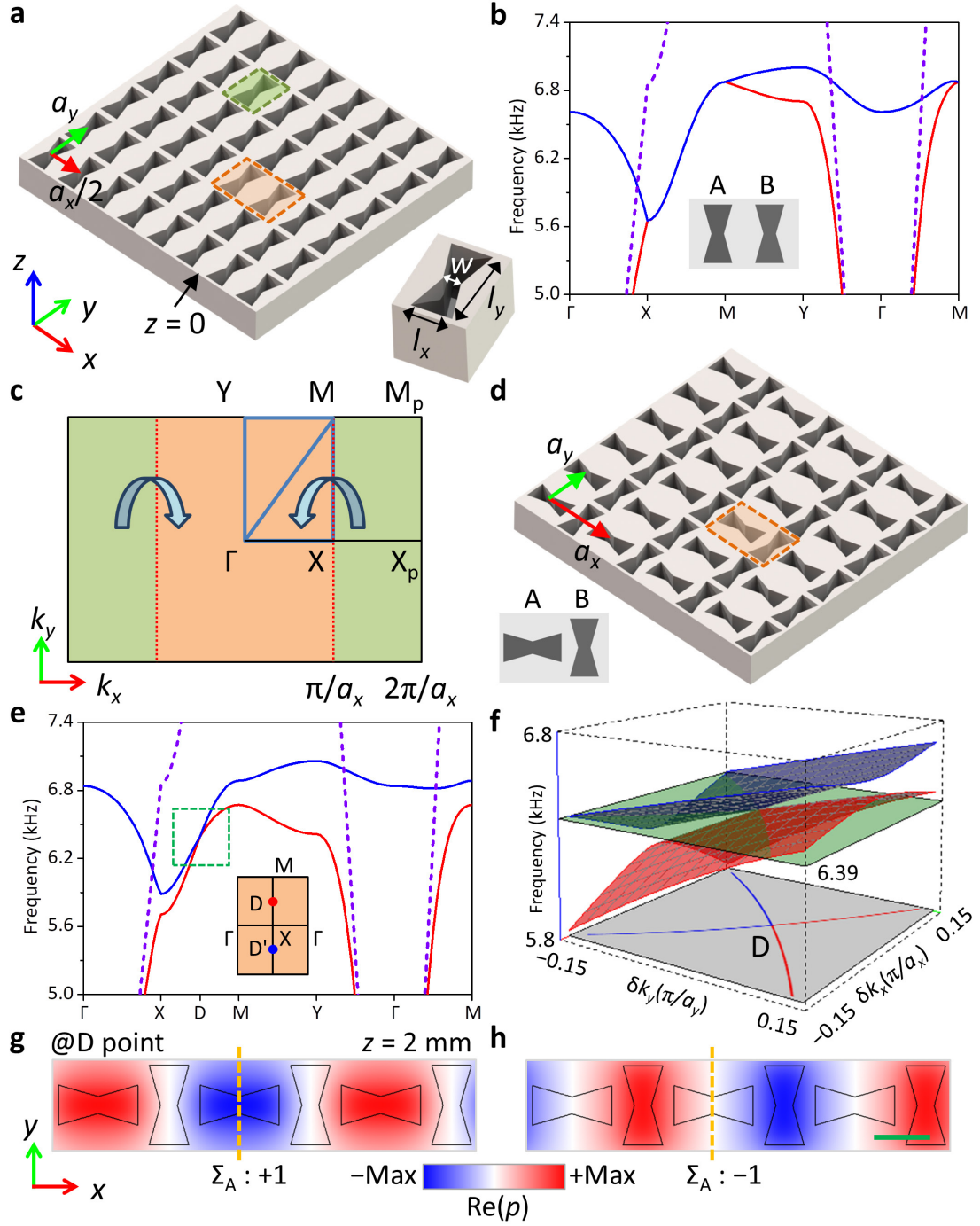


FIG. 1. Band-folding creation of type-II DPs. (a) Initial sonic crystal, an acoustic-hard plate drilled with bow-tie shaped holes arranged in a rectangular lattice. The green (orange) shaded region denotes a primitive (enlarged) unit cell. Inset: details of the primitive cell. (b) Calculated band structure of (a) based on the enlarged unit cell, comprising sublattices A and B labeled in the inset. Dashed lines: sound cone. (c)

Folding mechanism of the first Brillouin zone (FBZ) when considering an enlarged unit cell. Outer green region (XX_pM_pM) of the original FBZ are folded back into inner orange region (ΓXMY) along the fold line (XM). (d) Rotation (90°) of the left hole (sublattice A) in an enlarged unit cell transform it into a real unit cell (orange shaded region). Inset: schematic of the transformed unit cell. (e) Band structure of the sonic crystal in (d). The 1st (red) and 2nd (blue) bands linearly touch each other in midpoint D of the XM -direction, highlighted by the green dashed rectangle. Inset: distribution of type-II DPs in the Brillouin zone. Due to time-reversal symmetry, another inequivalent type-II DP exists at D' point. (f) 3D band structure around D point. At 6.39 kHz (the green, semi-transparent plane), its iso-frequency contour (IFC) features a pair of crossing lines contacting at D point. (g,h) Pressure fields of the doublet eigenmodes at D, corresponding to eigenvalues ± 1 of the mirror symmetry Σ_A indicated by orange dashed lines. The green scale bar is 10 mm.

Then, if we deliberately consider an enlarged unit cell (shaded orange region in Fig. 1(a)) comprising two primitive cells, the 1st band will be folded back [28]. The nominal “1st” and “2nd” bands are degenerate along the XM -direction (Fig. 1(b)), since it is exactly the fold line in the reciprocal space (Fig. 1(c)). Such degeneracy could serve as the basis for constructing type-II DPs, if we could lift the degeneracy along the line except a single point. The first step is to transform the enlarged unit cell into a “real” primitive unit cell. We decompose the enlarged unit cell into two sublattices, left holes A and right holes B (see inset in Fig. 1(b)), and rotate each hole

in sublattice A with 90° (Fig. 1(d)). Subsequently, the band structure (Fig. 1(e)) shows that the 1st and 2nd bands now only touch linearly at midpoint $D(\pi/a_x, -\pi/(2a_y))$ of the XM-direction, where a type-II DP emerges at the frequency $f_D = 6.39$ kHz, as highlighted by the green dashed rectangle. Due to time-reversal symmetry, they will also touch at the inequivalent $D'(\pi/a_x, -\pi/(2a_y))$ point, and the inset in Fig. 1(e) summarizes their distribution. The 3D band structure around D point (Fig. 1(f)) detailedly visualizes the point touch between the two bands. The pressure field maps of the two eigenmodes at D point (Figs. 1(g) and 1(h)) reveal that, the degenerate doublets, with fields localized around different sublattices, exhibit opposite parities with respect to the mirror symmetry Σ_A (yellow dashed lines), which ensures their orthogonality. Thus, the symmetric (anti-symmetric) eigenmode belongs to A_1 (A_2) representation of C_{2v} point group, and the type-II DPs only correspond to accidental degeneracies. However, the emergence and distribution of the type-II DPs are indeed insensitive to the shape and geometric parameters of the mirror-symmetric holes (see Fig. S2 for further examples, and Note S1 for advantage of bow-tie shape).

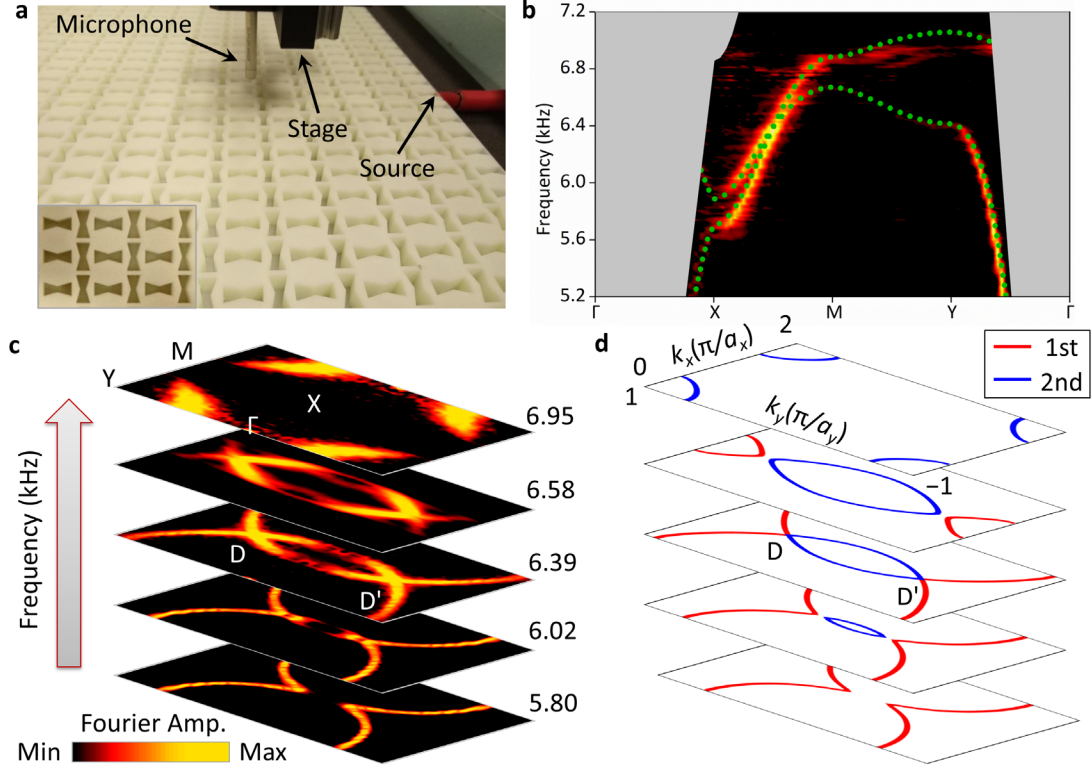


FIG. 2. Experimental imaging of type-II DPs. (a) Photograph of experimental setup for near-field mappings (see Note S11 for details [37].). Inset: close top-view of the 3D printed sample. (b) Fourier spectra along high-symmetry directions of the FBZ. Green dots indicate numerical dispersion. Only regions outside the sound cone are shown. (c) Fourier spectra at selected frequencies. Bright strips represent excited SSAW modes, indicating their IFCs in the reciprocal space. (d) Numerically calculated IFCs at corresponding frequencies. Type-II DPs manifest themselves as the contacts of the “electron-like” (red IFCs) and “hole-like” (blue IFCs) Fermi pockets. Note that a Brillouin zone is topologically equivalent to a torus [38].

Before investigating the mechanism, we first perform near-field mappings with 3D-printed samples to confirm our findings (experiment setup in Fig. 2(a), see Note S11 for details). From Fourier transforms of the mapped pressure fields, the Fourier

spectra along high-symmetry directions in the reciprocal space are retrieved (Fig. 2(b)). The bright strips signify the SSAW modes excited in experiments [39,40], whose dispersions agree excellently with the simulated one (green dots). Further, Fourier spectra in the whole Brillouin zone are stacked with increasing frequency (Fig. 2(c)), where the bright strips indicate the iso-frequency contours (IFCs) of the sonic crystal. The numerically calculated IFCs at corresponding frequencies are plotted for reference (Fig. 2(d)), and their evolutions agree quite well: when frequency increase, the number of closed IFCs, that is, Fermi pockets [1], changes from 1 to 2, and finally to 1 again. Amidst this transition, type-II DPs emerge as the contacts between the “electron-like” (1st band) and “hole-like” (2nd band) Fermi pockets [9,14,16,18].

To analytically investigate the mechanism, we employ a tight-binding model (Fig. 3(a)) since the s -orbital SSAW modes are well localized. We first only consider nearest-neighbor (NN) hoppings, including x -direction t_x , and y -direction t_{yA} and t_{yB} . From Fourier transforms on tight-binding Hamiltonian in the real space (see Note S11), we obtain the Hamiltonian $H(\mathbf{k})$ in the reciprocal space

$$H(\mathbf{k}) = \begin{bmatrix} \omega_0 - t_{yA}(e^{ik_y a_y} + e^{-ik_y a_y}) & -t_x(1 + e^{ik_x a_x}) \\ -t_x(1 + e^{-ik_x a_x}) & \omega_0 - t_{yB}(e^{ik_y a_y} + e^{-ik_y a_y}) \end{bmatrix}, \quad (1)$$

where ω_0 is the on-site angular frequency of both sublattices, and $\mathbf{k} = (k_x, k_y)$ is the Bloch wave vector. Around the midpoint $D(\pi/a_x, \pi/(2a_y))$ of XM-direction, we expand $H(\mathbf{k})$ with respect to the deviation $\delta\mathbf{k} = (\delta k_x, \delta k_y)$. To the first order, we have (see Note S2 for details [37])

$$H(D + \delta\mathbf{k}) = t_{ys} a_y \delta k_y \sigma_0 - t_x a_x \delta k_x \sigma_2 - t_{yd} a_y \delta k_y \sigma_3 + \omega_0 \sigma_0, \quad (2)$$

where σ_0 is the identity matrix and σ_i ($i = 1, 2, 3$) are Pauli matrices, with parameters $t_{ys} = t_{yA} + t_{yB}$ and $t_{yd} = t_{yB} - t_{yA}$. The Taylor-expanded Hamiltonian in Eq. (2) is identical to Hamiltonians of type-II DPs obtained from the lowest-order $\mathbf{k} \cdot \mathbf{p}$ method in previous works [9,14,16] up to unitary transformations. Due to the first tilt term, the Dirac cone at D point is tipped over towards +y direction, and since $|t_{ys}| \gg |t_{yd}|$, the tilt term dominates, resulting in a type-II DP [16,41]. To confirm this picture, we calculate the (angular) eigenfrequencies from Eq.(2),

$$\omega_{\pm}(\mathbf{D} + \delta\mathbf{k}) = \omega_0 + v_{ys}\delta k_y \pm \sqrt{(v_x\delta k_x)^2 + (v_{yd}\delta k_y)^2}, \quad (3)$$

where the sign + (−) denotes the 2nd (1st) band, and parameters $v_x = t_x a_x$, $v_{ys} = t_{ys} a_y$, and $v_{yd} = t_{yd} a_y$ characterize anisotropic group velocities (see Note S11 for fitting of the parameters [37]). As established in Eq. (3), which agrees well with numerical dispersions (Figs. 3(b) and 3(c)), the type-II DP is fixed at both deterministic location (D point) and frequency (ω_0). The conclusion, due to the mirror symmetry and identical on-site frequencies, is still valid after taking into account next-nearest-neighbor hoppings (see Notes S4 and S5).

To ensure this simple model has captured the essence of the deterministic scheme, we consider another sonic crystal comprising coupled resonant cavities [33]. Under similar perturbations, it also realizes type-II DPs (see Note S3 and Fig. S3). Therefore, if the bands of a rectangular (or square) lattice with mirror symmetry are twice folded along one direction, a strong tilt naturally arises at the corresponding FBZ boundary. Then, a pair of mirror-symmetry protected type-II DPs can emerge around midpoints of the FBZ boundary once we detune NN hoppings along the orthogonal “unfolded”

direction for each sublattice.

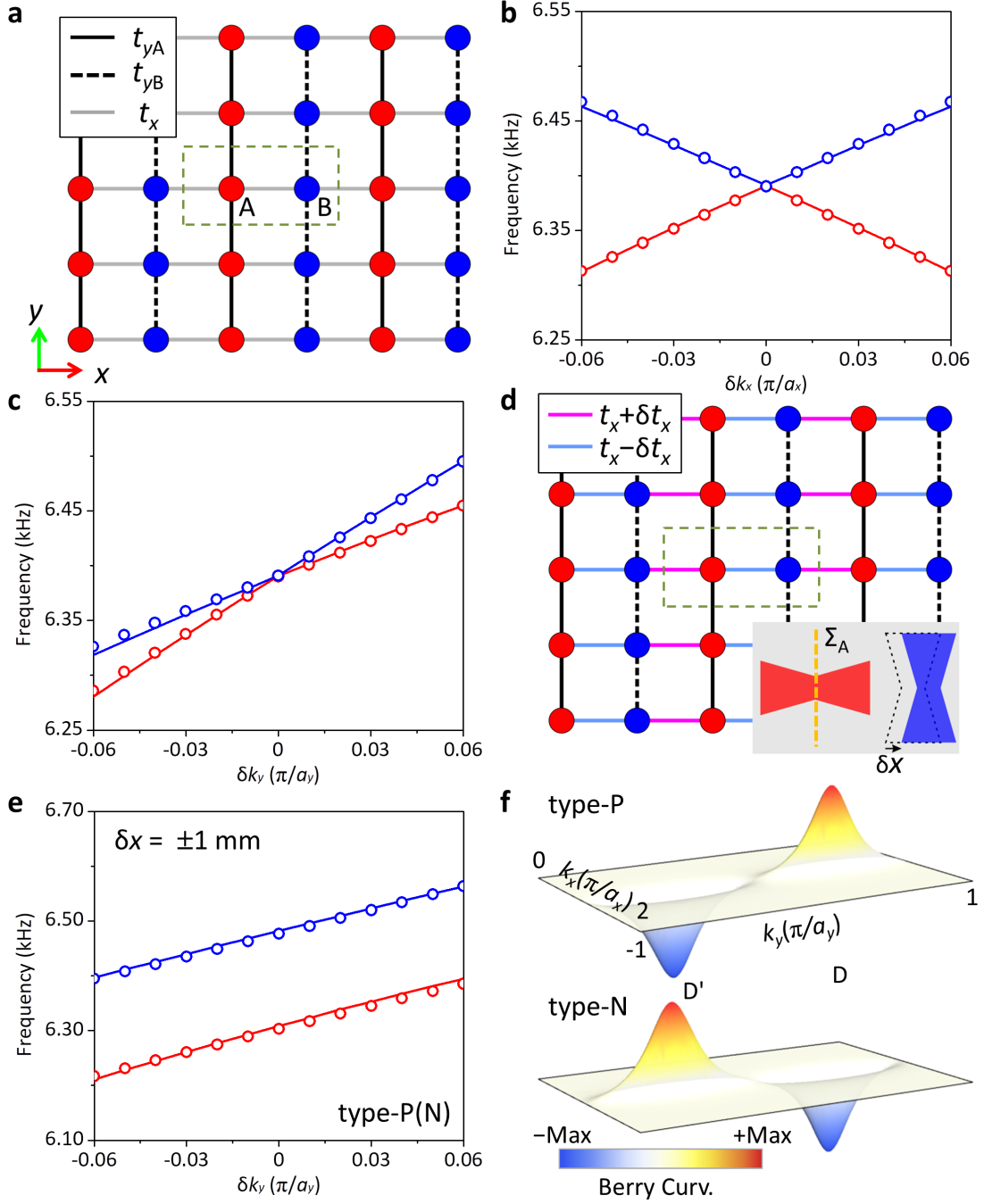


FIG. 3. Tight-binding analysis of band-folding mechanism. (a) Tight-binding model of the sonic crystal in Fig. 1(d). The s -orbital SSAW modes in sublattice A (B) are represented by red (blue) lattice points. Only nearest-neighbor (NN) hoppings are considered. (b,c) Band structure near the D point along the x direction (b) or y direction (c), calculated from simulations (solid lines) or tight-binding model (scatters)

in (a). (d) Tight-binding model of the sonic crystal when sublattice B is shifted with a displacement $\delta\mathbf{r} = (\delta x, 0)$. Inset: schematic of the displacement, which breaks mirror symmetry Σ_A and creates a hopping difference δt_x along the x direction. (e) Band structure near the D point along the y direction for type-P ($\delta x = +1$ mm) and type-N ($\delta x = -1$ mm) unit cells, calculated from simulations (solid lines) or tight-binding model (scatters) in (d). (f) Berry curvature distributions for type-P and type-N unit cells, calculated from tight-binding model in (d) (see Fig. S6 and Note S8 [37]).

For further corroboration, we examine a direct effect of the tipped-over Dirac cones: valley-Hall kink states (VHKs), induced by localized Berry curvatures of gapped type-II DPs, are so strongly tilted that they propagate along the same direction at each “valley” when hosted in opposite supercells. They may be termed type-II VHKs to distinguish from type-I VHKs induced by gapped type-I DPs [29,32,42,43], which propagate along the opposite directions when hosted in opposite supercells. To create type-II VHKs, we first introduce perturbations breaking mirror symmetry Σ_A which protects type-II DPs. Simply, we shift sublattice B with a displacement $\delta\mathbf{r} = (\delta x, 0)$, which introduces a hopping difference δt_x in x -direction (Fig. 3(d)), resulting in a mass term (see Note S6). We label a unit cell as type-P (type-N) if $\delta x > 0$ ($\delta x < 0$). The two opposite shifts $\delta\mathbf{r} = (\pm\delta x, 0)$ lead to identical band structures but opposite valley-Hall properties. Without loss of generality, we focus on the representing cases $\delta x = \pm 1$ mm. Again, the tight-binding model correctly depicts the band structure around D point (Fig. 3(e)), featuring a partial bandgap (see also Fig.

S4). Then, we calculate their 1st-band Berry curvatures $\Omega_{z,-}$ using a tight-binding Hamiltonian including the hopping difference (see Note S8). Anisotropic peaks emerge around D/D' point (Fig. 3(f)), where they can be approximated as (see Note S8)

$$\Omega_{zD/D',-}(\delta\mathbf{k}) = \pm \frac{v_x v_{yd} \Delta_p}{2[(v_x \delta k_x)^2 + (v_{yd} \delta k_y)^2 + \Delta_p^2]^{3/2}} \quad (4)$$

, in which $\Delta_p = 2\delta t_x$, and the sign $+$ ($-$) corresponds to D (D') point. Since the Berry curvatures are localized, it is possible to define half-quantized valley-Chern numbers [16,29,42] around D/D' point on half of the FBZ (HFBZ)

$$C_{V,-}^{D/D'} = \frac{1}{2\pi} \int_{\text{HFBZ}} \Omega_{zD/D',-} d^2\mathbf{k} = \pm \frac{1}{2} \text{sgn}(v_{yd} \Delta_p), \quad (5)$$

which is $+1/2$ ($-1/2$) for type-P (type-N) at D point, and reversed at D' point (see Note S8). For type-II VHKs, the positive (negative) differences of valley-Chern numbers indicate faster (slower) propagations, instead of forward (backward) propagations for type-I VHKs [29,42] (see Note S9 for derivations).

We then construct two possible supercells comprising a kink running along y direction, which we refer to as PN-configuration (Fig. 4(a)) and NP-configuration (Fig. 4(b)). Obviously, NP-configuration is the opposite of PN-configuration, and they cannot be transformed into each other through an $\text{SO}(3)$ operation. As shown in their projected band structures (Fig. 4(c)), strongly tilted type-II VHKs emerge in the partial bandgap, and their pressure fields (Figs. 4(d) and 4(e)) both demonstrate exponential decay profiles in the bulk domains (see Fig. S7 for detailed distributions). They also exhibit sublattice polarizations with their pressure fields almost exclusively localized in sublattice A or B (see Note S9 for derivations).

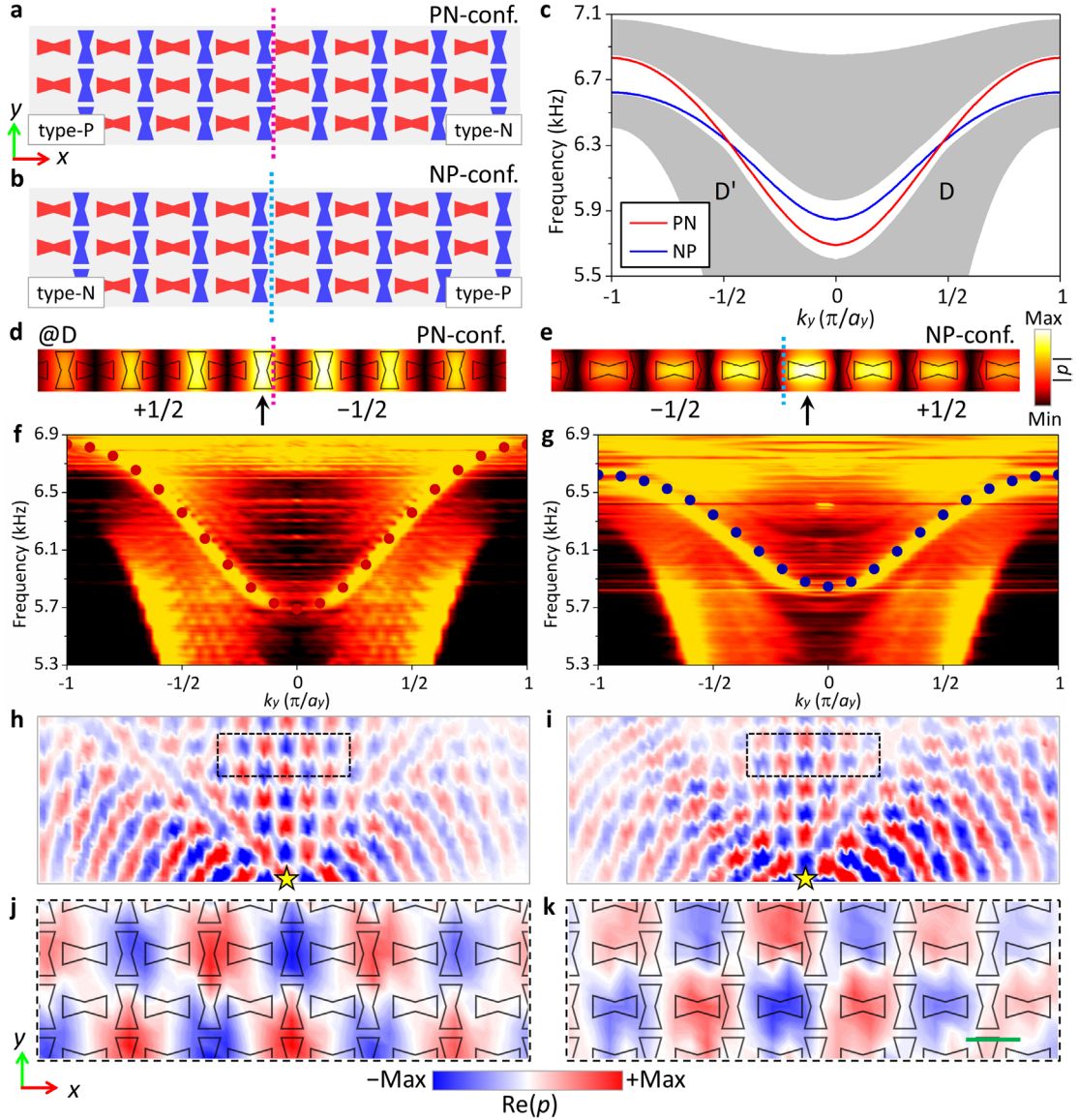


FIG. 4. Observation of type-II valley-Hall kink states (VHKs). (a,b) Schematics of supercells periodic along y direction, formed by type-P and type-N unit cells, referred to as PN-configuration (a) and NP-configuration (b), respectively. The dashed lines indicate kinks between the two domains. (c) Numerically calculated projected band structure. The gray shaded regions correspond to bulk bands. The type-II VHKs of PN-configuration (NP-configuration) is denoted by the red (blue) solid line. (d,e) Simulated pressure distributions of type-II VHKs at the projected D point ($k_y = \pi/(2a_y)$), for PN-configuration (d) and NP-configuration (e), respectively. The black

arrows indicate where the field is strongest. (f,g) Fourier spectra obtained from measured pressure field maps for PN-configuration (f) and NP-configuration (g), excited with matched sublattice polarizations. The dark red (blue) dots indicate the numerical dispersion of type-II VHKs in PN-configuration (NP-configuration). (h-i) Imaged pressure fields at 6.40 kHz for PN-configuration (h) and NP-configuration (i). Yellow stars indicate where source sounds are injected. (j,k) Enlarged views of selected areas enclosed by black dashed rectangles in (h,i), revealing sublattice polarizations of type-II VHKs in PN-configuration (j) and NP-configuration (k). The green scale bar is 16 mm.

Finally, we perform near-field mappings to detect the type-II VHKs. The spatial Fourier spectra (Figs. 4(f) and 4(g)), are retrieved from imaged pressure fields, and have been averaged over $\pm k_y$. They correspond to the PN-configuration and NP-configuration sample, respectively, both stimulated with matched sublattice polarizations (see Note S11 for details). In the spectra, the bright narrow strips clearly demonstrate the successfully excited type-II VHKs and they agree quantitatively with numerically calculated dispersions (dark red and blue dots). To visualize the excited states, We plot imaged field maps at 6.40 kHz (see Fig. S8 for other frequencies) for the PN-configuration (NP-configuration) sample in Fig. 4(h) (Fig. 4(i)). It is seen that type-II VHKs in both samples propagate along the $+y$ direction, alongside bulk states spreading laterally (see their time-harmonic animations Movies S1 and S2). Moreover, the pressure fields of type-II VHKs in PN-configuration

(NP-configuration) sample are largely localized in sublattice B (A), as displayed in their enlarged views (Figs. 4(j) and 4(k)), agreeing with predicted sublattice polarizations. When the samples are stimulated with mismatched sublattice polarizations, the type-II VHKs are much weakly excited (see Fig. S9 and Movies S3 and S4). For comparison, we have also imaged fields of a reference sample comprising only type-N unit cells, and only bulk bands are observed in both real and reciprocal spaces (see Fig. S10 and Movies S5 and S6).

Discussion

In this work, we propose and experimentally confirm a deterministic scheme for type-II DPs based on the band-folding mechanism. Realized in acoustics, the scheme is further understood through a general tight-binding model, and is potential to inspire construction and utilization of type-II DPs in other research areas, such as electronic materials and coupled photonic waveguides, which may lead to exotic phenomena and properties. The deterministic scheme may serve as a platform for investigating classical topological phenomena in the context of type-II DPs, including the Klein tunneling [23,24], the *Zitterbewegung* effect [25-27], synthetic Landau levels [34] and non-Hermitian physics [31]. It may also inspire more systematic designs for type-II WPs in 3D space. Moreover, by introducing an additional parameter, the scheme directly lead to type-II synthetic WPs (see Note S10). If more parameters are introduced, it could enable constructions of peculiar topological defects occurring at higher synthetic dimensions beyond the real space, and open the door for further

researches.

Acknowledgement

The work is supported by Hong Kong Research Grants Council (RGC) grants (AoE/P-02/12 and 16304717), Fundamental Research Funds for the Central Universities (2018CDXYWU0025 and 2018CDJDWL0011) from Ministry of Education of China, and Key Technology Innovation Project in Key Industry of Chongqing (cstc2017zdcy-zdyf0338).

References

- [1] A. A. Soluyanov, D. Gresch, Z. Wang, Q. Wu, M. Troyer, X. Dai, and B. A. Bernevig, Type-II weyl semimetals, *Nature* **527**, 495 (2015).
- [2] M. Goerbig, J.-N. Fuchs, G. Montambaux, and F. Piéchon, Tilted anisotropic Dirac cones in quinoid-type graphene and α -(BEDT-TTF)₂I₃, *Physical Review B* **78**, 045415 (2008).
- [3] M. Trescher, B. Sbierski, P. W. Brouwer, and E. J. Bergholtz, Quantum transport in Dirac materials: Signatures of tilted and anisotropic Dirac and Weyl cones, *Physical Review B* **91**, 115135 (2015).
- [4] L. Huang, T. M. McCormick, M. Ochi, Z. Zhao, M.-T. Suzuki, R. Arita, Y. Wu, D. Mou, H. Cao, and J. Yan, Spectroscopic evidence for a type II Weyl semimetallic state in MoTe₂, *Nature Materials* **15**, 1155 (2016).
- [5] T. O’Brien, M. Diez, and C. Beenakker, Magnetic breakdown and Klein tunneling in a type-II Weyl semimetal, *Physical Review Letters* **116**, 236401 (2016).
- [6] A. Frenzel, C. Homes, Q. Gibson, Y. Shao, K. Post, A. Charnukha, R. J. Cava, and D. Basov, Anisotropic electrodynamics of type-II Weyl semimetal candidate WTe₂, *Physical Review B* **95**, 245140 (2017).
- [7] N. Kumar, Y. Sun, N. Xu, K. Manna, M. Yao, V. Süß, I. Leermakers, O. Young, T. Förster, and M. Schmidt, Extremely high magnetoresistance and conductivity in the type-II Weyl semimetals WP₂ and MoP₂, *Nature Communications* **8**, 1642 (2017).
- [8] F. Fei, X. Bo, R. Wang, B. Wu, J. Jiang, D. Fu, M. Gao, H. Zheng, Y. Chen, and X. Wang, Nontrivial Berry phase and type-II Dirac transport in the layered material PdTe₂, *Physical Review B* **96**, 041201 (2017).
- [9] M. Horio, C. Matt, K. Kramer, D. Sutter, A. Cook, Y. Sassa, K. Hauser, M. Månsson, N. Plumb, and M. Shi, Two-dimensional type-II Dirac fermions in layered

- oxides, *Nature Communications* **9**, 3252 (2018).
- [10] J. Lai, X. Liu, J. Ma, Q. Wang, K. Zhang, X. Ren, Y. Liu, Q. Gu, X. Zhuo, and W. Lu, Anisotropic Broadband Photoresponse of Layered Type - II Weyl Semimetal MoTe₂, *Advanced Materials* **30**, 1707152 (2018).
- [11] K.-W. Chen, X. Lian, Y. Lai, N. Aryal, Y.-C. Chiu, W. Lan, D. Graf, E. Manousakis, R. Baumbach, and L. Balicas, Bulk Fermi Surfaces of the Dirac Type-II Semimetallic Candidates M Al₃ (Where M= V, Nb, and Ta), *Physical Review Letters* **120**, 206401 (2018).
- [12] Z. Yang and B. Zhang, Acoustic Type-II Weyl Nodes from Stacking Dimerized Chains, *Physical Review Letters* **117**, 224301 (2016).
- [13] H.-X. Wang, Y. Chen, Z. H. Hang, H.-Y. Kee, and J.-H. Jiang, Type-ii dirac photons, *npj Quantum Materials* **2**, 54 (2017).
- [14] G. G. Pyrialakos, N. S. Nye, N. V. Kantartzis, and D. N. Christodoulides, Emergence of type-II Dirac points in graphynelike photonic lattices, *Physical Review Letters* **119**, 113901 (2017).
- [15] C.-R. Mann, T. J. Sturges, G. Weick, W. L. Barnes, and E. Mariani, Manipulating type-I and type-II Dirac polaritons in cavity-embedded honeycomb metasurfaces, *Nature Communications* **9**, 2194 (2018).
- [16] C. Hu, Z. Li, R. Tong, X. Wu, Z. Xia, L. Wang, S. Li, Y. Huang, S. Wang, and B. Hou, Type-II Dirac Photons at Metasurfaces, *Physical Review Letters* **121**, 024301 (2018).
- [17] J. Noh, S. Huang, D. Leykam, Y. D. Chong, K. P. Chen, and M. C. Rechtsman, Experimental observation of optical Weyl points and Fermi arc-like surface states, *Nature Physics* **13**, 611 (2017).
- [18] J. Y. Lin, N. C. Hu, Y. J. Chen, C. H. Lee, and X. Zhang, Line nodes, Dirac points, and Lifshitz transition in two-dimensional nonsymmorphic photonic crystals, *Physical Review B* **96**, 075438 (2017).
- [19] Q. Guo, B. Yang, L. Xia, W. Gao, H. Liu, J. Chen, Y. Xiang, and S. Zhang, Three dimensional photonic Dirac points in metamaterials, *Physical Review Letters* **119**, 213901 (2017).
- [20] B. Xie, H. Liu, H. Cheng, Z. Liu, S. Chen, and J. Tian, Experimental Realization of Type-II Weyl Points and Fermi Arcs in Phononic Crystal, *Physical Review Letters* **122**, 104302 (2019).
- [21] Z. Liu, Q. Zhang, F. Qin, D. Zhang, X. Liu, and J. J. Xiao, Type-II Dirac point and extreme dispersion in one-dimensional plasmonic-dielectric crystals with off-axis propagation, *Physical Review A* **99**, 043828 (2019).
- [22] T. Ozawa, H. M. Price, A. Amo, N. Goldman, M. Hafezi, L. Lu, M. Rechtsman, D. Schuster, J. Simon, and O. Zilberberg, Topological photonics, *Reviews of Modern Physics* **91**, 015006 (2019).
- [23] O. Bahat-Treidel, O. Peleg, M. Grobman, N. Shapira, M. Segev, and T. Pereg-Barnea, Klein tunneling in deformed honeycomb lattices, *Physical Review Letters* **104**, 063901 (2010).
- [24] X. Ni, D. Putseladze, D. A. Smirnova, A. Slobozhanyuk, A. Alù, and A. B. Khanikaev, Spin-and valley-polarized one-way Klein tunneling in photonic

- topological insulators, *Science Advances* **4**, eaap8802 (2018).
- [25] X. Zhang, Observing Zitterbewegung for photons near the Dirac point of a two-dimensional photonic crystal, *Physical Review Letters* **100**, 113903 (2008).
- [26] F. Dreisow, M. Heinrich, R. Keil, A. Tünnermann, S. Nolte, S. Longhi, and A. Szameit, Classical simulation of relativistic Zitterbewegung in photonic lattices, *Physical Review Letters* **105**, 143902 (2010).
- [27] W. Ye, Y. Liu, J. Liu, S. A. Horsley, S. Wen, and S. Zhang, Photonic Hall effect and helical Zitterbewegung in a synthetic Weyl system, *Light: Science & Applications* **8**, 49 (2019).
- [28] L.-H. Wu and X. Hu, Scheme for achieving a topological photonic crystal by using dielectric material, *Physical Review Letters* **114**, 223901 (2015).
- [29] X. Wu, Y. Meng, J. Tian, Y. Huang, H. Xiang, D. Han, and W. Wen, Direct observation of valley-polarized topological edge states in designer surface plasmon crystals, *Nature Communications* **8**, 1304 (2017).
- [30] Z. Zhang, Q. Wei, Y. Cheng, T. Zhang, D. Wu, and X. Liu, Topological Creation of Acoustic Pseudospin Multipoles in a Flow-Free Symmetry-Broken Metamaterial Lattice, *Physical Review Letters* **118**, 084303 (2017).
- [31] M. Wang, L. Ye, J. Christensen, and Z. Liu, Valley Physics in Non-Hermitian Artificial Acoustic Boron Nitride, *Physical Review Letters* **120**, 246601 (2018).
- [32] J. Noh, S. Huang, K. P. Chen, and M. C. Rechtsman, Observation of Photonic Topological Valley Hall Edge States, *Physical Review Letters* **120**, 063902 (2018).
- [33] X. Ni, M. Weiner, A. Alù, and A. B. Khanikaev, Observation of higher-order topological acoustic states protected by generalized chiral symmetry, *Nature Materials* **18**, 113 (2019).
- [34] X. Wen, C. Qiu, Y. Qi, L. Ye, M. Ke, F. Zhang, and Z. Liu, Acoustic Landau quantization and quantum-Hall-like edge states, *Nature Physics*, 1 (2019).
- [35] D. Torrent and J. Sánchez-Dehesa, Acoustic analogue of graphene: observation of Dirac cones in acoustic surface waves, *Physical Review Letters* **108**, 174301 (2012).
- [36] S. Yves, R. Fleury, F. Lemoult, M. Fink, and G. Lerosey, Topological acoustic polaritons: robust sound manipulation at the subwavelength scale, *New Journal of Physics* **19**, 075003 (2017).
- [37] See Supplementary Material at [inserted URL], for 1) Effects of hole shapes and advantages of bow-ties, 2) Expansion of Hamiltonians around type-II DPs, 3) Realization of type-II DPs using coupled resonant cavities, 4) Tight-binding model taking into account further neighbor hoppings, 5) Shift and annihilation of type-II DPs when sublattices are detuned, 6) Hamiltonians and eigenfrequencies when mirror symmetry is broken, 7) Numerical calculation of Berry curvatures, 8) Analytical calculation of Berry curvatures and valley Chern numbers, 9) Analytical derivation of type-II VHKSs and sublattice polarizations, 10) Construction of synthetic type-II Weyl points, and 11) Methods in the studies.
- [38] L. Lu, J. D. Joannopoulos, and M. Soljačić, Topological photonics, *Nature Photonics* **8**, 821 (2014).
- [39] J. Lu, C. Qiu, L. Ye, X. Fan, M. Ke, F. Zhang, and Z. Liu, Observation of topological valley transport of sound in sonic crystals, *Nature Physics* **13**, 369 (2016).

- [40]F. Li, X. Huang, J. Lu, J. Ma, and Z. Liu, Weyl points and Fermi arcs in a chiral phononic crystal, *Nature Physics* **14**, 30 (2018).
- [41]S. Li, Z.-M. Yu, Y. Liu, S. Guan, S.-S. Wang, X. Zhang, Y. Yao, and S. A. Yang, Type-II nodal loops: Theory and material realization, *Physical Review B* **96**, 081106 (2017).
- [42]F. Gao, H. Xue, Z. Yang, K. Lai, Y. Yu, X. Lin, Y. Chong, G. Shvets, and B. Zhang, Topologically protected refraction of robust kink states in valley photonic crystals, *Nature Physics* **14**, 140 (2018).
- [43]L. Ju, Z. Shi, N. Nair, Y. Lv, C. Jin, J. Velasco Jr, C. Ojeda-Aristizabal, H. A. Bechtel, M. C. Martin, and A. Zettl, Topological valley transport at bilayer graphene domain walls, *Nature* **520**, 650 (2015).